

THE HYDROGEN EPOCH OF REIONIZATION ARRAY DISH: CHARACTERIZATION WITH ELECTROMAGNETIC SIMULATIONS

EWALL-WICE AARON^{1,2}, RICHARD BRADLEY^{3,4}, ABRAHAM NEBEN^{1,2}, NIPANJANA PATRA⁵, THYAGARAJAN NITHYANANDAN⁶,
 JACQUELINE HEWITT^{1,2}, ALI S. ZAKI⁵, BOWMAN JUDD⁶, CHENG CARINA⁵, DEBOER DAVID⁵, PARSONS AARON⁵, VENTER
 MARIET⁷ AND OTHERS.

Draft version January 13, 2016

ABSTRACT

Using electromagnetic simulations, we assess the spectral properties of the antenna element of the Hydrogen Epoch of Reionization Array (HERA) in order to both establish a specification for the degree of spectral structure that is permissible to sufficiently isolate foregrounds and allow a detection of the cosmological 21 cm signal and verify direct laboratory measurements of the dish characteristics. We find that our simulations are in good agreement with field measurements. Using simulations of foregrounds, we find that the ≈ -40 dB response at 60 ns of the HERA dish is sufficient to isolate the cosmological 21 cm signal $\approx 0.2 h\text{Mpc}^{-1}$ at $z \approx 8.5$ and obtain a high signal to noise detection of the power spectrum. This study represents the first time that direct measurements a 21 cm interferometer design have been translated into its ability to constrain the physics of reionization.

1. INTRODUCTION

Observations of the redshift 21 cm radiation neutral hydrogen in the intergalactic medium (IGM) have the potential to illuminate the hitherto unobserved *dark ages* and *cosmic dawn*, revolutionizing our understanding of the first UV and X-ray sources in the universe and how their properties influenced galactic evolution (see Furlanetto et al. (2006), Morales & Wyithe (2010), and Pritchard & Loeb (2012) for reviews). As of now, two major experimental endeavors are underway to make a first detection of the 21 cm signal with most focusing on the Epoch of Reionization (EoR) in which UV photons from early galaxies transformed the hydrogen in the universe from neutral to ionized. The first involves measuring the sky-averaged global signal and is being pursued by experiments such as EDGES (Bowman & Rogers 2010), LEDA (Greenhill & Bernardi 2012), DARE (Burns et al. 2012), SciHi (Voytek et al. 2014), and BIGHORNS (Sokolowski et al. 2015) coming online in their planning stages or taking data. The second attempts to observe spatial fluctuations in the 21 cm emission using radio interferometers. As of now, a first generation of interferometry experiments are taking data in an attempt to make a first statistical detection of the power spectrum of 21 cm brightness temperature fluctuations. These include the Giant Metrewave Telescope (GMRT) (Paciga et al. 2013), the Low Frequency Array (LOFAR), (van Haarlem et al. 2013), the Murchison Widefield Array (?) and the Precision Array for Probing the Epoch of Reionization (PAPER) (Parsons et al. 2010).

The primary obstacle to obtaining a high redshift detection of the cosmological signal through both of these methods is the existence of foregrounds that are

$\sim 10^5 - 10^6$ times brighter. While requiring much greater sensitivity to global-signal experiments, interferometers have the advantage that these spectrally smooth foregrounds naturally avoid a significant region of k -space, known as the *EoR window*, occupying a region known as the *wedge* (Datta et al. 2010; Vedantham et al. 2012; Parsons et al. 2012; Thyagarajan et al. 2013; Liu et al. 2014a,b), however any structure in the frequency response of the instrument has the potential to leak foregrounds into the EoR window, masking our signal. Indeed, low level spectral structures in the analogue and digital signal chains on the initial buildout of the MWA are proving to be a significant obstacle (Dillon et al. 2015; Ewall-Wice et al. submitted 2015; Beardsley et al. in preparation).

While, in principle, spectral structure in the band-pass of the instrument may be removed in calibration, simulations show that any mismodeling of emission and the primary beam, potentially below the confusion limit, will mix the significant spectral structure on long baselines into short ones, masking the signal entirely (Barry et al. in preparation). While redundant calibration (Wieringa 1992; Liu & Tegmark 2011; Zheng et al. 2014) is able to calibrate the independent of a detailed model of the sky, any direction-dependent chromatic structure in the primary beam of the instrument introduces additional degrees of freedom that must be modeled, potentially leading to signal loss and the introduction of spurious spectral structure due to unmodeled foregrounds in long baselines. Because of our limited knowledge of foregrounds at low-frequency and the fidelity of calibration algorithms, the only sure way of building an instrument that will guarantee a detection of the redshifted 21 cm emission is to design it such that all spectral structure in the signal chain is limited to a finite region of delay space, well below the wedge.

The Hydrogen Epoch of Reionization Array (HERA) is an instrument currently taking first observations in the Karoo in South Africa with the ultimate goal of detecting the power spectrum of 21 cm brightness temperature fluctuations at high signal-to-noise (SNR) (Pober

¹ MIT Kavli Institute for Cosmological Physics

² MIT Dept. of Physics

³ National Radio Astronomy Obs., Charlottesville VA

⁴ Dept. of Astronomy, U. Virginia, Charlottesville VA

⁵ Astronomy Dept. U. California, Berkeley CA

⁶ School of Earth and Space Exploration, Arizona State U., Tempe AZ

et al. 2014). A central principle in HERA’s design is that it be calibration fail-safe such that a detection of the signal is guaranteed, even if the chromaticity of the instrument is not calibrated out. This paper and its companions (Neben et al. submitted; Patra et al. submitted; Thyagarajan et al. submitted) describe a multifaceted approach to establishing a stringent specification on the spectral structure permissible for HERA to be calibration fail-safe and determine to what extent its design meets these requirements. We accomplish this by establishing a spec with simulations of foregrounds (?) and verifying that HERA primary antenna element meets this spec with reflectometry (Patra et al. submitted) and Or-bcomm beam mapping (Neben et al. submitted). These measurements are verified with detailed electromagnetic simulations which we describe in this work.

This paper is organized as follows. In § 2 we lay out our analytic framework for describing the impact of reflections and spectral structure on foreground leakage in delay-transform power spectra. In § 3 we describe our electromagnetic simulations of the HERA dish element. In § 4 we compare our simulation results to direct measurements of the primary dish element and in § ?? we apply our electromagnetic simulation results to simulations of foregrounds to determine the extent that the HERA dish’s chromatic structure pollutes the EoR window and their impact on HERA’s overall sensitivity. We conclude in § 6.

2. THE IMPACT OF REFLECTIONS ON DELAY-TRANSFORM POWER SPECTRA

In this section, we show how reflections in the analogue signal path of an antenna lead to foreground contamination of the EoR window. Intuitively, any reflections in the signal path introduce sinusoidal ripples in the frequency dependent gain of the instrument. Since reflection delay is the Fourier dual to frequency, reflections at larger delays introduce ripples at higher frequencies. Isolation of the 21 cm signal from foregrounds that are over five orders of magnitude brighter depends critically on their smoothness. Any sinusoidal frequency structure, introduced by the antenna gain will cause these foregrounds to mimic and swamp the signal unless they are brought below a level similar to the ratio between the foregrounds and the signal itself. We now derive this process in formal detail. A simple equation for effect of direction independent reflections in the signal chain of an interferometer, downstream of the receiver, has been derived in Ewall-Wice et al. (submitted 2015), we extend this analysis in this section by considering the direction dependent reflections that can occur within the antenna element. We assume that the intensity field on the sky is given by

$$I(\hat{\mathbf{k}}, f) \delta_D(\hat{\mathbf{k}} - \hat{\mathbf{k}}') = \langle s(\hat{\mathbf{k}}, f) s^*(\hat{\mathbf{k}}', f) \rangle_t^2 \quad (1)$$

where δ_D is the Dirac delta function and $\langle \rangle_t$ indicates an average in time. We imagine that the electric field as a function of time, $\tilde{s}(\hat{\mathbf{k}}, t)$ arrives at an arbitrary origin at time t and at the various i^{th} antenna elements of an interferometer at locations \mathbf{x}_i at times $\tau_i = \mathbf{x}_i \cdot \hat{\mathbf{k}}/c$. We now consider reflections within a single dish element described by a direction dependent reflection coefficient⁷,

$\tilde{r}_i(\hat{\mathbf{k}}, \tau)$. which re-introduce the signal at later times τ . The voltage signal measured at the i^{th} antenna element, \tilde{v}_i , is the integral over solid angle of the convolution of the electric field entering the antenna (delayed by τ_i) with $r_i(\hat{\mathbf{k}}, \tau')$.

$$\tilde{v}_i(t) = \int d\Omega \int d\tau \tilde{r}_i(\hat{\mathbf{k}}, \tau) \tilde{s}(\hat{\mathbf{k}}, t - \tau_i - \tau) \quad (2)$$

A correlator (FX and XF) measures the time-averaged product of the Fourier transform of the voltage streams between the i^{th} and j^{th} antenna. Fourier transforming the voltage stream from the i^{th} antenna we obtain

$$v_i(f) = \int d\Omega \int d\tau \tilde{r}_i(\hat{\mathbf{k}}, \tau) s(\hat{\mathbf{k}}, f) e^{-2\pi i f(\tau_i + \tau)} \quad (3)$$

The time averaged product between the two antennas is

$$V'_{ij}(f) = \langle v_i(f) v_j^*(f) \rangle_t = \int d\Omega \int d\tau \tilde{r}_i(\tau) d\tau' \tilde{r}_j^*(\tau') e^{-2\pi i f(\tau - \tau')} I(\hat{\mathbf{k}}, f) \quad (4)$$

where $\Delta\tau_{ij} = \tau_i - \tau_j = (\mathbf{x}_i - \mathbf{x}_j) \cdot \hat{\mathbf{k}}/c$. We eliminated one of the solid angle integrals using equation 1.

Defining $\mathbf{u}_{ij} = f(\mathbf{x}_i - \mathbf{x}_j)/c$, we obtain,

Then the resulting visibilities obtained by cross correlating antenna i and antenna j are given by

$$V'_{ij}(f) = \int d\Omega r_i(\hat{\mathbf{k}}, f) r_j^*(\hat{\mathbf{k}}, f) I(f, \hat{\mathbf{s}}) e^{2\pi i f \mathbf{u}_{ij} \cdot \hat{\mathbf{k}}/c}, \quad (5)$$

where $\mathbf{b}_{ij} = (\mathbf{x}_i - \mathbf{x}_j)$ to use the usual uv notation of interferometry. $r_i(\hat{\mathbf{k}}, f)$ is the inverse fourier transform of the reflection response of the dish, hence we see that the reflection response is precisely the Fourier dual to the Dish’s frequency domain voltage beam. Setting a specification on reflections is hence equivalent to setting a specification on the spectral smoothness of the voltage beam.

In order to separate spectrally smooth foregrounds from our signal, we expect to use the *delay transform* over frequency, defined as (Parsons et al. 2012)

$$\tilde{V}_{ij}(\tau) = \int df e^{2\pi i \tau f} V_{ij}(f) \quad (6)$$

Applying this to equation 5, we obtain

$$\tilde{V}'_{ij}(\tau) = \int d\Omega \int df r_i(\hat{\mathbf{k}}, f) r_j^*(\hat{\mathbf{k}}, f) I(f, \hat{\mathbf{k}}) e^{2\pi i f(\mathbf{b}_{ij} \cdot \hat{\mathbf{k}}/c - \tau)} \quad (7)$$

Let’s examine the quantity within the angular integral. For each $\hat{\mathbf{k}}$, we see that each source is mapped to a line $\tau = \mathbf{b}_{ij} \cdot \hat{\mathbf{k}}/c$, resulting in the much discussed “wedge” (Datta et al. 2010; Vedantham et al. 2012; Parsons et al. 2012; ?; Thyagarajan et al. 2013; Liu et al. 2014a,b). The presence of the frequency dependent beam causes each source line to be convolved in delay with the direction dependent kernel

$$\tilde{R}_{ij}(\hat{\mathbf{k}}, \tau) = \int d\tau' \tilde{r}_i(\hat{\mathbf{k}}, \tau - \Delta\tau) \tilde{r}_j^*(\hat{\mathbf{k}}, -\Delta\tau). \quad (8)$$

which is the convolution of the delay response of voltage beam i with the complex conjugate of voltage beam j evaluated on a negative t-axis, $\tilde{r}_i(\hat{\mathbf{k}}, \tau), \tilde{r}_j^*(\hat{\mathbf{k}}, \tau)$. Note

⁷ Ignoring reflections between multiple dish elements which we treat in Appendix A

that this is not equal to the convolution of the voltage response with its complex conjugate, which would lead to foreground power only being bled out to positive delays. Usually, beams have a different delay structure in each direction, and we demonstrate the effect of foreground smearing in Fig. 1 for a simple model with only three sources. Without reflections, the sources would form lines in $b - \tau$ space. With the reflections, the sources are smeared out, leading to supra-horizon emission. For the sake of pedagogy, we now consider the case where the beam can be factored into angular and frequency dependent components, $r_i(\hat{\mathbf{k}}, f) = g_i(f)a_i(\hat{\mathbf{k}})$. For such a case, every line in Fig. 1 would be convolved with the same delay dependent shape, normalized to the gain of $a_i(\hat{\mathbf{k}})$. In this case, we have

$$\tilde{V}_{ij}(\tau) = \int d\tau' \int d\tau'' \tilde{g}_i(\tau' - \tau'') \tilde{g}_j^*(\tau'') \tilde{V}_{ij}(\tau - \tau') \quad (9)$$

We can further simplify matters by assuming that $\tilde{g}_i(\tau = 0) \gg \tilde{g}_i(\tau > 0)$, which is often a good assumption at large delays for the relatively smooth bandpasses our instruments are designed to have.

$$\tilde{V}'_{ij}(\tau) \approx \tilde{g}_i(0) \int d\tau' \tilde{g}_j^*(\tau') \tilde{V}_{ij}(\tau - \tau') + \tilde{g}_j^*(0) \int d\tau' \tilde{g}_i(\tau') \tilde{V}_{ij}(\tau - \tau') \quad (10)$$

Hence, to first order, the impact of reflections is to convolve the delay-transformed visibility with the voltage beam of the instrument, which acts as the power-kernel. This may be a somewhat un-intuitive result since we might naively expect for the power-kernel to be the square of the delay-response. This linear falloff puts exquisite requirements on the smoothness of the beam, requiring that it fall roughly six orders of magnitude in delay before the signal is accessible.

In this paper, we derive $\tilde{r}_i(\hat{\mathbf{k}}, \Delta\tau)$ for the HERA antenna element using electromagnetic simulations, in order to verify direct measurements of the antenna element with refelctometry (Patra et al. submitted) and Orbcomm measurements of the beam (Neben et al. submitted). We also explore the implications of the HERA dish's $\tilde{r}_i(\hat{\mathbf{k}}, \tau)$ on the scientific bottom line for EoR, using the Fisher Matrix Formalism.

3. ELECTROMAGNETIC SIMULATIONS OF THE HERA DISH ELEMENT

In Fig. 2 we show the geometry of the electromagnetic simulation. **Rich: fill in the details here**

3.2. Deconvolving the Response Function

Since our simulation is sampled in finite time steps, we will adopt discretized notation for this section. In particular, our simulation consists of N samples, evenly spaced by $d\tau$ at times $\tau_n = n \times d\tau$. In our simulation, we obtain the voltage at the feed output at time τ_n which we will call \tilde{v}_n . It is related to the input plane wave through the discrete convolution

$$\tilde{v}_n(\hat{\mathbf{k}}) = \sum_m \tilde{r}_m(\hat{\mathbf{k}}) \tilde{s}_{n-m}(\hat{\mathbf{k}}), \quad (11)$$

We may undo this convolution by taking a discrete Fourier transform (DFT) of both $\tilde{\mathbf{v}}$ and $\tilde{\mathbf{s}}$ in time, dividing them in Fourier space, and taking an inverse DFT

back. Symbolically,

$$\tilde{\mathbf{r}}(\hat{\mathbf{k}}) = \mathcal{F}^{-1} \left[\frac{\mathcal{F}\tilde{\mathbf{v}}(\hat{\mathbf{k}})}{\tilde{\mathbf{s}}(\hat{\mathbf{k}})} \right] \quad (12)$$

where \mathcal{F} is the Fourier transform matrix for a 1d vector of length N .

$$\mathcal{F}_{mn} = e^{2\pi i mn/N} \quad (13)$$

In Fig. 4 we show the amplitude of the Fourier transform of our Gaussian input, centered at 150 MHz along with the voltage response. Since our input is band limited between ≈ 20 and 280 MHz, the direct ratio of our voltage response and input wave is dominated by numerical noise outside of this range. We eliminate these numerical artifacts by multiplying our ratio by a Blackman-Harris window between 100 MHz and 200 MHz and set our estimate to zero elsewhere. From a physical standpoint, this is sensible since 21 cm experiments only observe a limited bandwidth. PAPER's correlator, which will initially serve as the HERA backend samples over a 100 MHz instantaneous frequency interval. Hence analogue filtering is applied to limit the incoming signal within a finite bandwidth and prevent aliasing.

We plot the delay transform of the voltage response of the dish in Figure 5 to gauge the dynamic range of our simulations. Since signal at negative delays violates causality, we assume such features are sourced by numerical artifacts such as side-lobes and/or numerical precision noise. We see that our simulations have a dynamic range of -60 dB.

3.3. The Delay Response of Subbands

While we observe a long term falloff due to reflections between the feed and dish element, it is possible that these reflections are localized in frequency and do no effect certain sub-bands. To determine whether the reflections are localized in frequency, we compute the voltage delay response and power kernel for three different subbands: 100 – 130 MHz, 130 – 160 MHz, and 160 – 190 MHz. In order to maintain decent resolution of the kernel itself, we use frequency ranges are larger than the actual subbands that will be used for EoR power spectrum estimation ~ 10 MHz which is set by the interval over which the statistics of the cosmological HI signal are expected to be stationary. We plot the delay transforms of the voltage gain in Fig. 8 and the power kernels in Fig. 9. The central lobe of the delay kernel is significantly wider due to the the wider window functions incurred by the reduced bandwidth, however, the shallow long-term falloff is only visible within the central 125 – 175 MHz band, indicating that long term reflections are isolated near 150 MHz and will not effect power spectrum measurements outside of the very center of our band.

3.4. Extrapolating the Bandpass and Power Kernel

Our deconvolution gives us the time-domain voltage response of the PAPER and HERA antenna elements. We plot the absolute value of this response in Fig. ??, seeing that it drops to -30 dB after ≈ 100 ns. The power-kernel that convolves visibilities to higher delays is the convolution of $\tilde{r}(\tau)$ with its time-reversed complex conjugate,

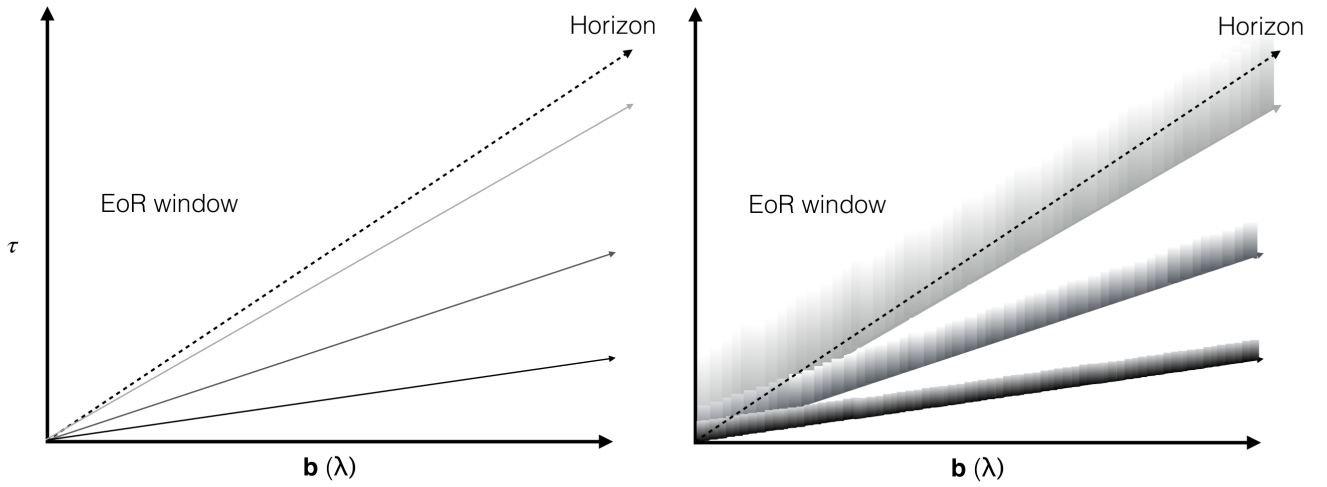


FIG. 1.— We demonstrate the impact on foregrounds of the frequency dependent beam. Left: The location of three sources in delay space assuming a frequency independent beam (no reflections in the antenna element). Right: the presence of chromaticity due to reflections in the antenna smears the source in delay with the kernel given by equation 8. Since the frequency response of the dish are a function of direction on the sky, the shape of the delay kernel is different for each source line. We see that this smearing can lead to substantial supra-horizon emission. Sources near zenith (low delay) tend to have a larger maximum since the beam gain is larger near zenith, but a more compact kernel (since beam bore-sights tend to have less spectral structure). Meanwhile, sources near the horizon have a much smaller maxima but have less compact kernels.

3.1. The Simulations

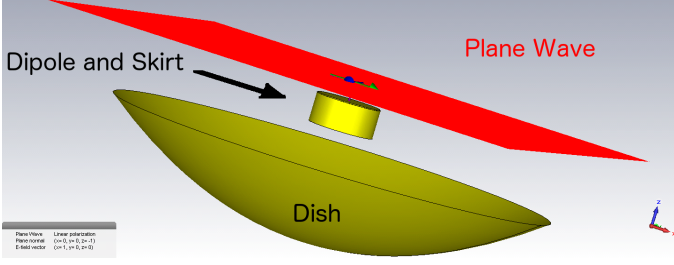


FIG. 2.— A rendering of our time domain simulation at $t = 0$, demonstrating the geometry and setup of our electromagnetic simulation. The plane wave is started just above the feed (red plane).

which we plot as the red line. The convolution is in very good agreement with the voltage response itself which is explained by the fact that second order terms of the convolution, approximately given by $|\tilde{r}(\tau)|^2$ (green line) are over two orders of magnitude smaller above 50 ns.

Our simulations of the Dish response only extend to ≈ 300 ns, however, we wish to understand the impact of reflections on the frequency dependent gain of an interferometer like HERA at comoving scales of $\approx 0.1 - 0.5 h\text{Mpc}^{-1}$, corresponding to the delays between 180 and 900 ns at $z = 8$, extending beyond our simulations range. To extrapolate out to higher delays, we assume that the response function is dominated by reflections between the feed and the dish. This is due to the fact that when we extend our filter bandwidth to between 50 and 250 MHz and use a hamming window (which has higher resolution), we observe lobe-like structures at delays beyond 100 ns with a periodicity of 30 ns, which corresponds to the round-trip light travel time between the feed and the dish. In addition, the long term falloff appears as a line on a linear-log plot (Fig. 5), indicating that the kernel follows an exponential which we now show is indicative of reflections. We do so by adopting the notation of (Patra et al. submitted). We let Γ_d represent the reflection coefficient of the Dish vertex and Γ_f represent the reflection coefficient of the feed. An electromagnetic wave incident on the feed, at $t = 0$, is accepted with amplitude $(1 - \Gamma_f)$. The reflected component travels back to the dish and acquires an amplitude of $(\Gamma_f \Gamma_d)$ before returning at time, τ_d later where $(1 - \Gamma_f)$ will be accepted and so forth. The time dependent voltage at the feed from these reflections is thus

$$\tilde{v}_r(t) = \sum_m (\Gamma_f \Gamma_d)^m \tilde{s}(t - m\tau_d) \quad (14)$$

Hence

$$\tilde{r}_r(\tau) = \sum_m (\Gamma_f \Gamma_d)^m \delta_D(\tau - m\tau_d) \quad (15)$$

Since the number of reflections, $m = t/\tau_d$, than we can write the long-term delay response in discrete form as

$$\tilde{r}_n \approx (\Gamma_f \Gamma_d)^{nd\tau/\tau_d} \quad (16)$$

which is a power law. We thus model our discrete voltage response beyond the times sampled by our simulations as a power law

$$\tilde{r} = A X^{(\tau/30\text{ns})} \quad (17)$$

We plot the best power-law fit as a dashed line in Fig ??.

4. COMPARISON TO REFLECTOMETRY DATA

4.1. The Delay Response at Zenith

In Fig. 7, we show the filtered response function deconvolved from our electromagnetic simulations. The response of the dish rapidly dies off as a function of time. After ≈ 90 ns, we observe lobed structures with a period of ≈ 30 ns which corresponds to the geometrical delay between the feed and the dish apex, indicating that the large τ roll off is dominated by reflections between the feed and the dish.

Our simulations are intended to verify direct reflectometry measurements taken on a prototype of the HERA feed and dish in Green Bank, presented in (Patra et al. submitted). For the readers convenience, we briefly explain the reflectometry measurement here before comparing them to our simulation.

In the reflectometry measurement, a signal is sent from a Vector Network Analyzer (VNA) via a coaxial cable (which is calibrated out) into the back of the feed. The VNA then measures the ratio between returned and transmitted power as a function of frequency, $S_{11}(f)$. A fundamental difference between the reflectometry measurement and the delay response that we are attempting to obtain is that at zero delay, S_{11} is measuring the reflection of the input wave off of the back of the feed while in the delay response of the antenna, the zero delay reflection is the fraction of the electromagnetic wave off of the sky that is accepted by the feed. To obtain $\hat{\rho}$, we must correct for this difference. It is shown in (Patra et al. submitted) that the correction is

$$\hat{\rho}(f) = \frac{\Gamma_a(f)}{1 - \Gamma_a(f)} [S_{11}(f) - \Gamma_a(f)] + 1 - \Gamma_a(f). \quad (18)$$

Applying this transformation to $S_{11}(f)$ and taking a DFT into the time domain over a band of 100 – 200 MHz, we obtain a measurement based estimate of the dish response function at zenith which is plotted in Fig. 7 alongside our simulation result. The general trends of the two lines agree within $\sim 1 - 3$ dB. As the long term delay structure of the delay response determines to what extent foregrounds leak out of the wedge, our simulations verify our measurement of the HERA dish's key performance feature.

4.2. Comparison with the power kernel of the PAPER antenna element

We next compare the spectral characteristics of the HERA dish to the PAPER antenna element. The PAPER antenna consists of a sleeved dipole element identical to the one inside of the HERA feed. However, rather than being suspended over a dish which greatly enhances the effective collecting area of the antenna, the dipole is placed facing upwards above a rectangular skirt structure that is designed to minimize spectral structure. Comparing the relative performances of these two configurations is important since by suspending the dipole upside down over a dish, HERA is potentially trading achromaticity for collecting area. Here we comment this tradeoff. In order to perform a comparison, we run an identical plane wave simulation of the PAPER dipole element and obtain the power kernel which is shown in Fig. 7. The striking difference between the PAPER and

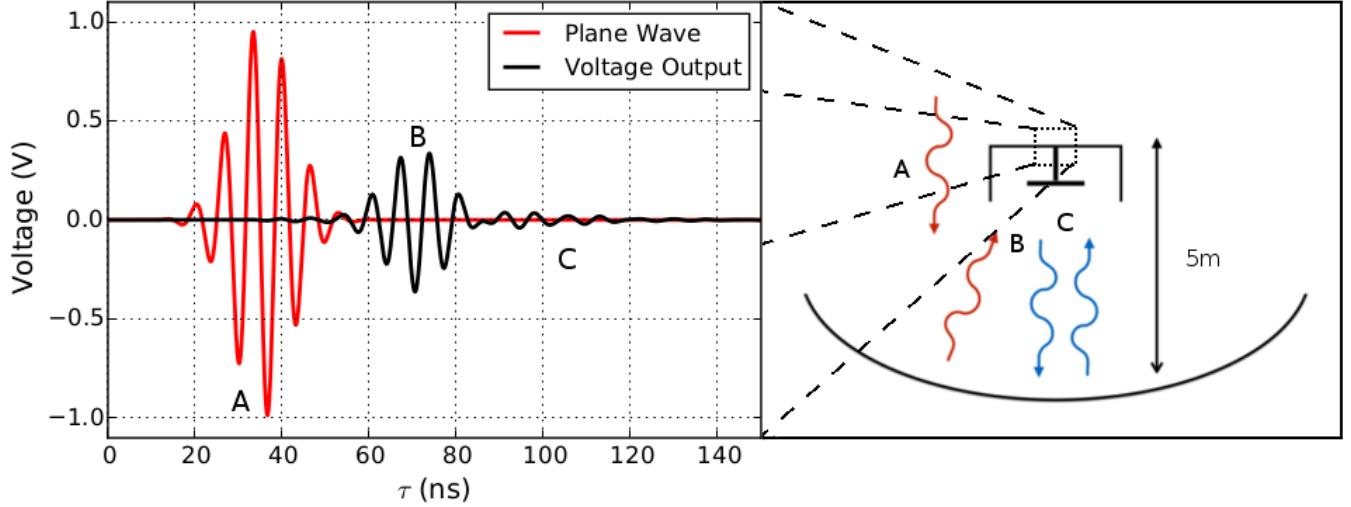


FIG. 3.— An illustration of our simulation products and their origin in the HERA antenna geometry. A plane wave is injected from above the feed (red line). The amplitude of the electric field of the plane wave at output of the feed along with the voltage at the feed terminal outputs is recorded (black line). The feed in our simulation is situated 5 m above the bottom of the dish, hence there is a ≈ 30 ns delay between when the plane wave passes the terminal for the first time (A) and when it is first absorbed in the dipole (B), leading to the voltage response. Of concern to 21 cm experiments are the subsequent reflections between the feed and the dish (C) which can lead to large delay contamination of the EoR window.

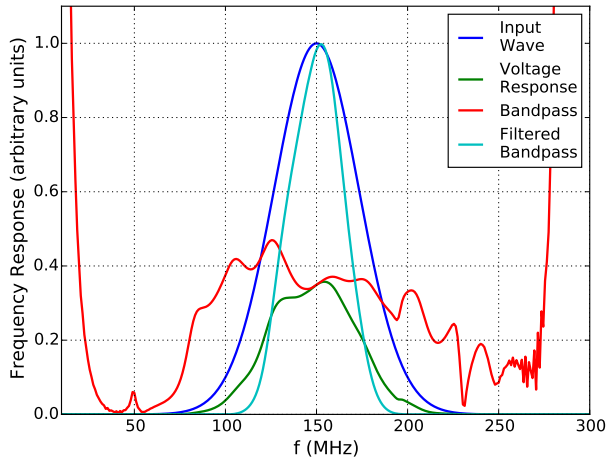


FIG. 4.— The absolute value of the discrete Fourier transform of our simulation outputs. We obtain the effective response function of the dish by Fourier transforming the voltage output from our dish (green line) and dividing by the Fourier transform of the input wave (blue line). The simple ratio is plotted as a red line. Since our input is limited to frequencies between ≈ 20 and 280 MHz, there is significant numerical noise that will effect our result outside of this region which we see in the divergence of the red line towards the edges of the plot. To eliminate this noise, we multiply by a Blackman-Harris window between 50 and 250 MHz and set our estimate to zero elsewhere. The Fourier transform of our response estimate with the filter applied is shown as a cyan line.

HERA elements is that the PAPER kernel lacks the transition to a shallow falloff at ~ 100 ns which we should expect given that the long term falloff is likely due to feed-dish reflections. **I am here!**

5. THE EFFECT OF THE HERA DISH CHROMATICITY ON FOREGROUND LEAKAGE AND SENSITIVITY

Having a thorough understanding of how the chromatic beam of the HERA dish leaks foregrounds into higher delays and a decent picture of the relevant voltage response of the dish itself, we are now in a position to explore the

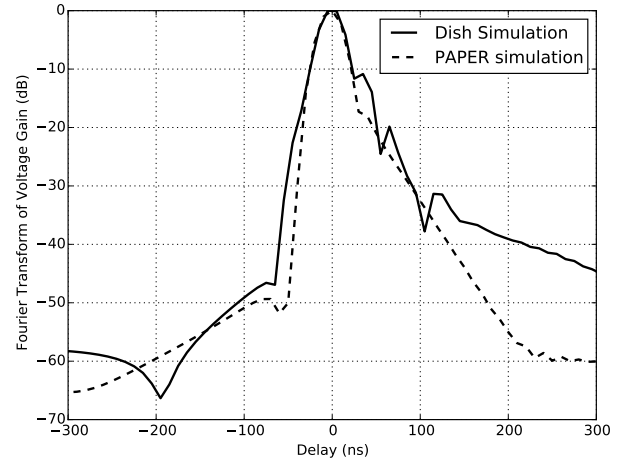


FIG. 5.— The Fourier transform of the voltage response function of our simulation for the HERA Dish (solid black line) and the PAPER antenna element (dashed black line). Reflections in the HERA dish element lead to significantly enhanced power above ~ 50 ns. We show the negative delays, which should be devoid of signal, to determine the dynamic range of our technique (which is limited by sidelobes and numerical artifacts). We see that these contaminants exist at the ~ -60 dB level.

impact of the Dish's performance on the leakage of foregrounds beyond the wedge, and into the EoR window. Beyond the delay kernels considered in this paper and (Patra et al. submitted), the extent of leakage will depend both on the angular structure of the primary beam, which is established in (Neben et al. submitted) and the model of the foregrounds themselves. In this section, we investigate the amplitude of foreground leakage as a function of delay given an angular primary beam model and our simulation of the delay structure of the dish (§ 5.1).

Spectral leakage due to the chromaticity of the dish will cause large-scale LoS Fourier modes to be contaminated by foregrounds and hence inaccessible to the foreground filtering approach that HERA will employ. Since the

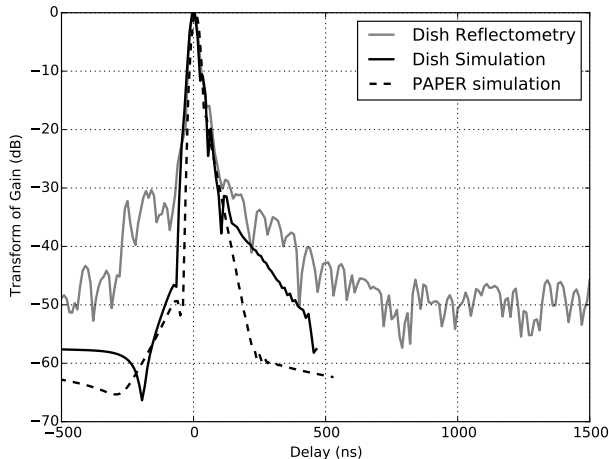


FIG. 6.— Same as Fig. 5 but now including the reflectometry measurements of (Patra et al. submitted). Inspecting negative delays, we see that the reflectometry measurements contain artifacts introduced by reflections and sub-reflections in the cables leading from the VNA to the feed which enter both the HERA dish and PAPER measurements at both the -45 dB to -30 dB level. The VNA measurement is noise dominated beyond ~ 500 ns.

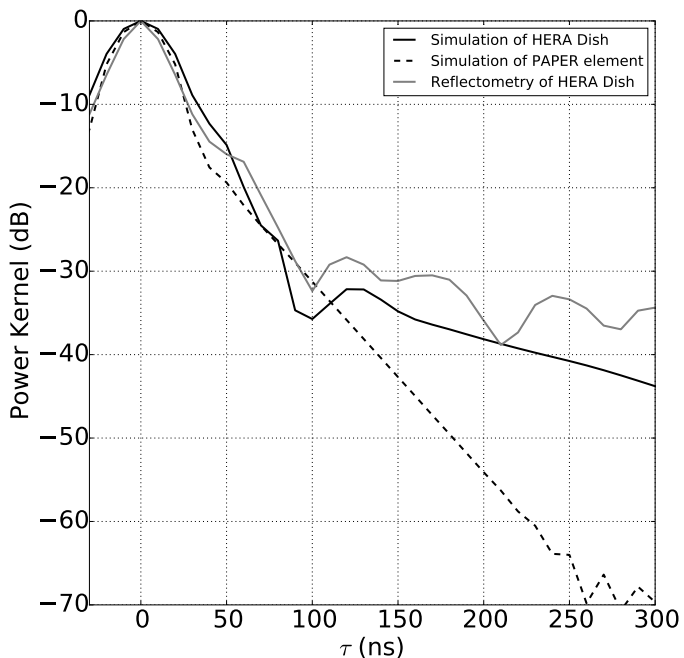


FIG. 7.— The response function deconvolved from our simulations (solid lines) compared to the response function estimated from reflectometry measurements described in (Patra et al. submitted) for the HERA dish and the PAPER antenna element. Our simulations agree well with the reflectometry results out to ≈ 100 ns but disagree by $\lesssim 10$ dB beyond this. A potential source of the disagreement is uncalibrated structure or irregularities in the cables connecting the Vector Network Analyzer and the antenna feed which enter at the -50 dB to -30 dB level.

signal-to-noise ratio is maximized at the smallest k values, the loss of these modes will reduce the significance of the power spectrum detection and negatively impact the overall bottom line of the science that HERA can accomplish. We explore the impact of HERA's intrinsic beam chromaticity on science using the Fisher matrix formalism in § ??.

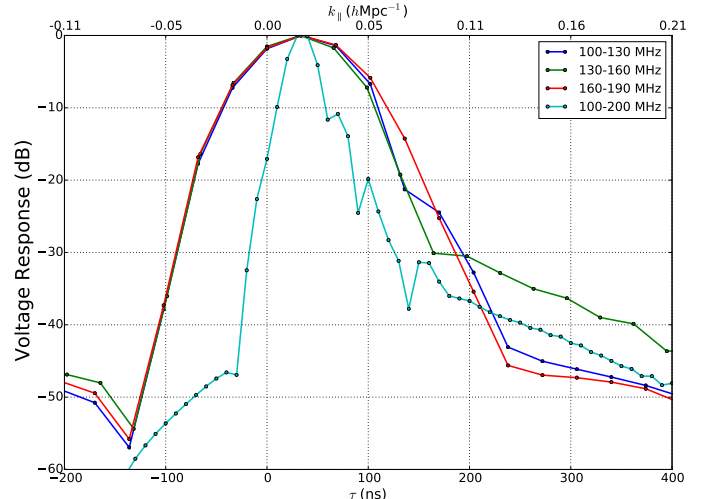


FIG. 8.— The delay transform of the voltage response of the HERA dish for the full 100 MHz bandwidth (cyan line) along with three subbands; 100–130 MHz, 130–160 MHz, and 160–190 MHz. The shallow falloff observed in § 3 is most prominent in the 130–160 MHz subband while the falloff in the other subbands is close to the level of the sidelobes (at ~ -50 dB for the lower resolution subbands). $k_{||}$ values for each delay are computed at 150 MHz.

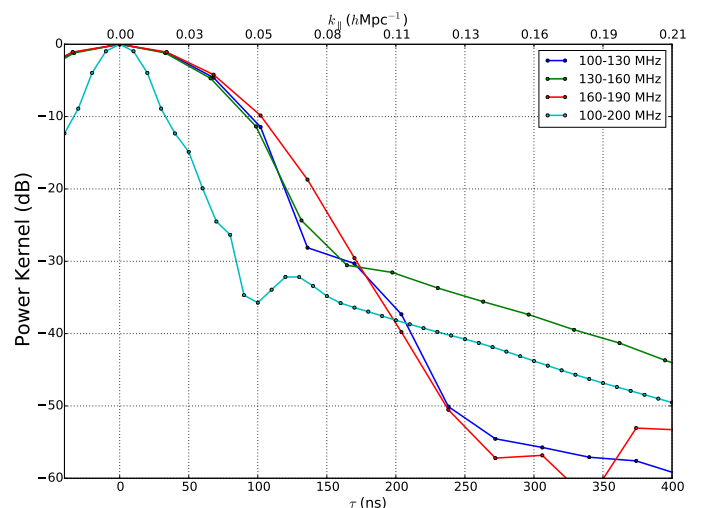


FIG. 9.— The power kernel for the three subbands discussed in in § 3.3 along with the kernel for the full bandwidth response function. While the long term falloff from reflections is prominent between 130–160 MHz, it appears at a much lower level in the other two subbands which fall below the central subband by ~ 20 dB at ~ 300 ns. $k_{||}$ values for each delay are computed at 150 MHz. The wider central lobe below 150 ns for the subband gains is an artifact of the delay resolution of a smaller bandwidth.

5.1. The Impact of the HERA Beam Chromaticity on Foreground Contamination

Given the HERA dish chromaticity, what Fourier modes will still be accessible with the delay filtering technique? To answer this question, we combine our extrapolated simulations of the HERA dish's spectral structure with simulations of foregrounds. The foreground simulations are described fully in (Thyagarajan et al. submitted) but for the readers convenience we briefly describe them here.

Our foreground model consists of two major components: diffuse synchrotron emission from our Galaxy

whose structure is described by the Global Sky Model (GSM) of ? and a population of point sources sourced by radio loud AGN which combines the NRAO Sky Survey (NVSS) (?) at 1.4 GHz, the Sydney University Mologolo Sky Survey (SUMMS) (?) at 843 MHz, and extrapolate point source fluxes to the observed 100-200 MHz band using a spectral index of $\langle\alpha\rangle = -0.83$ determined in ?. Visibilities are computed from the diffuse and point source models assuming the achromatic HERA beam computed at 150 MHz and described in (?). We compute two sets of visibilities: one in which the spectral structure of the dish is assumed to be completely flat, and another in which the beam is multiplied by the Dish's frequency dependent gain at zenith. While this model assumes incorrectly that the frequency evolution of the primary beam is identical along all lines of sight, the majority of power enters at the beams point of maximal gain (zenith) and observations of autocorrelations which reflect the angular average of the frequency dependence of all lines of sight agree well with our simulations at zenith (Patra et al. submitted).

The foreground filtering procedure employed by PAPER and HERA involves delay transforming the visibilities on a short time-scale cadence and performing a 1d delay CLEAN where the deconvolution is permitted to discover and subtract foregrounds within the horizon to horizon delay. Since we want to avoid CLEANing noise, the level of foreground subtraction possible by this procedure is limited by the thermal noise level on the visibility, which in turn depends on the number of time steps and redundant baselines that are averaged before performing the cleaning step. In this work, we assume that each visibility is cleaned independently with a two minute CLEANing cadence which corresponds approximately to the time over which HERA's short baselines are coherent. The standard deviation on the real and imaginary part of a single delay transformed visibility is given by (Morales & Hewitt 2004)

$$\Delta V = \frac{\sqrt{2k_B T_{sys}}}{A_e \sqrt{\tau}} \quad (19)$$

where A_e is the effective area of the dish, B is the bandwidth, T_{sys} is the system temperature, τ is the integration time, and k_B is the Boltzmann constant. The system temperature can be calculated by assuming that $T_{sys} = 100\text{K} + T_{sky}$ where 100 K is the temperature of the PAPER receiver and $T_{sky} = 60(\lambda/1\text{ meter})^{2.55}$ is the sky temperature (?). For A_e we use the value of 75 m determined in (Neben et al. submitted). If we assume that each baseline is cleaned independently and that the integration time is $\tau \approx 60\text{ s}$, then the noise level at 150 MHz is approximately 9.9 Jy MHz. In order to avoid subtracting noise, we assume that cleaning is performed down to 5σ . In Fig 10 we compare the delay transform of visibilities before and after cleaning on a two minute cadence at the LST of 4 hours. While cleaning is able to remove structure within the horizon, it does not reduce any of the power associated with the foreground induced by the chromaticity of the dish.

To form estimates of the 21 cm power spectrum, we split each visibility into BlackmanHarris windowed subbands centered at redshift intervals of $\Delta z = 0.5$ and each with an equivalent bandwidth of 10 MHz, corresponding

to the redshift interval over which the statistics of the brightness temperature fluctuations are expected to be stationary. For each windowed interval, we use the flat sky approximation and Fourier transform in frequency, square, and multiply by a set of prefactors to obtain a power spectrum estimate (?),

$$\hat{P}(\mathbf{k}) = \left(\frac{2k_B}{\lambda^2}\right)^2 \frac{X^2 Y}{B\Omega_{pp}} |\tilde{V}(\mathbf{u})|^2. \quad (20)$$

Here, λ is the central wavelength of the observation, k_B is the Boltzmann constant, B is the bandwidth of the Fourier transform, and Ω_{pp} is the integrated solid angle of the primary beam squared. X is a linear factor converting between uv wavelengths and k_\perp , and Y is a linear factor converting between k_\parallel and the Fourier dual to frequency, η .

A drift scan instrument, HERA will be capable of observing the sky at any LST within the strip declination that passes through its primary beam. To form a final power spectrum estimate, it is expected to perform an average over the power spectrum estimates it obtains through equation 20 for each LST independently. It is well documented that foreground power is maximized over certain LST ranges (Thyagarajan et al. 2015b), hence such an estimate will either filter or weight appropriately the LSTs in which foreground power is maximized. Thyagarajan et al. (submitted) focuses on the optimal weighting and selection of LST bins in forming a power spectrum estimate. For the purposes of our analysis, we focus on a single, relatively clean LST of 4 hours which includes the coldest part of the sky.

Computing the power spectra, we inspect the amplitude of foregrounds given the chromaticity and angular pattern of the HERA dish for several different baselines of different lengths.

5.2. The Implications of Dish Reflections on EoR Science

The primary goal 21 cm EoR observations is to obtain information about the nature of the sources that drove reionization. Since the amplitude of the 21 cm signal is maximal at smaller k values, a loss of large scale signal due to foreground leakage eliminates the modes that HERA would otherwise have the greatest signal to noise detections, impacting our overall sensitivity and its ability to derive this information. In this section, we estimate the impact of foreground leakage on HERA's sensitivity along with its ability to determine the astrophysics of reionization. We do so using the Fisher Matrix formalism. The Fisher Matrix allows us to forecast the covariances and errors on reionization parameters given errors on power spectrum observations due to the uncertainties caused by thermal noise which is in turn determined by the uv coverage and observing time of the interferometer. The covariance between the parameters of some model θ is given by the inverse of the Fisher matrix, \mathbf{F} which for Gaussian and independently determined power spectrum bins may be written approximately as (Poher et al. 2014; Ewall-Wice et al. submitted 2015),

$$F_{ij} \approx \sum_{k,z} \frac{1}{\sigma^2(k,z)} \frac{\partial \Delta^2(k,z)}{\partial \theta_i} \frac{\partial \Delta^2(k,z)}{\partial \theta_j}, \quad (21)$$

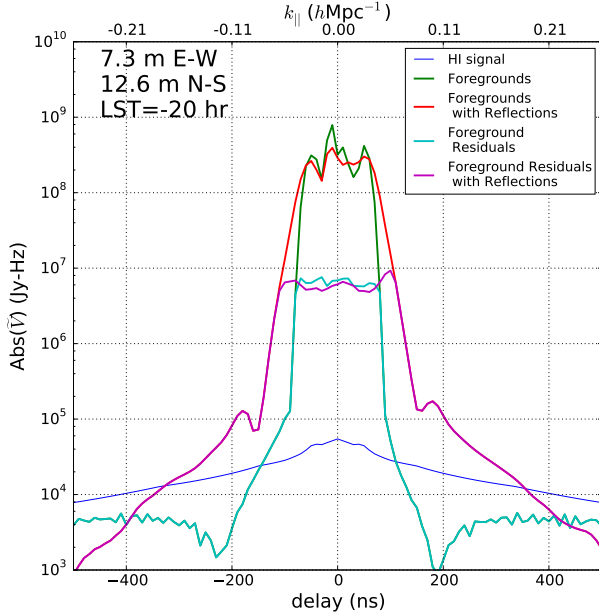


FIG. 10.— The absolute magnitude of a delay transformed 14-meter baseline (blue line) compared to the same visibility (green line) contaminated by reflections at the level observed in the HERA dish design. We see that the extended delay kernel smooths out structure, originating from foregrounds, within the horizon. For HERA, we expect to use the delay-clean to remove foregrounds. However, the depth of cleaning is limited by the noise level on a single baseline (black line). We show the foreground residuals with arising from a clean down to the 5σ noise level after 2 minutes of integration, seeing that cleaning at this cadence achieves \approx two orders of magnitude of foreground reduction. The reflections in the dish lead to extensive winged structures that bleed into the EoR window and are well below the thermal noise level. All data in this plot are obtained from a 100 MHz bandwidth centered at 150 MHz. Vertical dashed lines indicate the horizon delays of the baseline.

where $\Delta^2(k, z)$ is the power spectrum amplitude for some $k - z$ bin and $\sigma^2(k, z)$ is the variance of the power spectrum estimate in that bin due to thermal noise and cosmic variance (?).

we use the publicly available 21cmFAST code (?) which generates realizations of the 21 cm brightness temperature field using the excursion set formalism of ?. We employ a popular three parameter model of reionization (Pofer et al. 2014; ?; ?) with the following variables

- ζ : The “ionization efficiency” is defined in the (?) excursion formalism to be the inverse of the mass collapse fraction necessary to ionize a region and is computed from a number of other physical parameters such as the fraction of collapsed baryons that form stars and the UV photon escape fraction.

Because ζ acts as an efficiency parameter, its primary affect is to change the timing of reionization. We choose a fiducial value of $\zeta = 20$, though its possible values range anywhere between 5 and 50.

- R_{mfp} : The presence of Lyman limit systems and other potential absorbers within HII regions causes UV photons to have a mean free path denoted by R_{mfp} . In the 21cmFAST framework, HII regions cease to grow after reaching the radius of R_{mfp} , primarily impacting the morphology of the signal. We choose a fiducial value of $R_{\text{mfp}} = 15$ Mpc which is in line with recent simulations accounting for the subgrid physics of absorption (?).
- $T_{\text{vir}}^{\text{min}}$: The minimal mass of dark matter halos that hosted ionizing sources. While in principle, halos with virial temperatures as small as 10^2 K are though, in principle, to be able to form stars, thermal and mechanical feedback have been seen to raise this limit to as high as 10^5 K. We choose a fiducial value of $T_{\text{vir}}^{\text{min}} = 1.5 \times 10^4$ K which is set by the atomic line cooling threshold.

In order to account for the degeneracies in the power spectrum between heating from X-rays and reionization from UV photons, we also marginalize over three additional parameters that describe the impact of heating from early X-ray luminous sources as explored in (?). These are the X-ray heating efficiency f_X , the maximal energy of X-ray photons that are self absorbed by the ISM of early galaxies, ν_{min} , and the spectral slope, α which are taken to have fiducial values of 1, 0.3 keV, and -1.2 respectively. We choose to parameterize our model in terms of the fractional differences of each parameter from their fiducial values so that, for example, $\theta_\zeta = (\zeta - \zeta_{\text{fid}})/\zeta_{\text{fid}}$ and compute the derivatives in equation by performing a linear fit to realizations of the 21 cm power spectrum calculated by 21cmFAST at $\theta_i = \pm 10^{-2}, \pm 5 \times 10^{-2}, \pm 10^{-1}, \text{ and } \pm 2 \times 10^{-2}$.

What about $\sigma^2(k, z)$? σ^2 represents the noise on each 1 dimensional power spectrum estimate. For each measurement in the uv plane, the standard deviation of a power spectrum measurement is given by the direct sum of sample variance and thermal noise (?) which in turn depends on the primary beam of the instrument and the time spent sampling each uv cell. For our analysis, we assume that the uv plane is sampled by circular apertures with effective areas of 75 m^2 and that $\tau(\mathbf{k})$ is determined by a drift scan in which baselines are integrating coherently on each uv cell for ≈ 20 minutes.

6. CONCLUSIONS

REFERENCES

- Barry et al. in preparation
 Beardsley et al. in preparation
 Bowman, J. D., & Rogers, A. E. E. 2010, *Nature*, 468, 796
 Burns, J. O., et al. 2012, *Advances in Space Research*, 49, 433
 Datta, A., Bowman, J. D., & Carilli, C. L. 2010, *ApJ*, 724, 526
 Dillon, J. S., et al. 2015, *Phys. Rev. D*, 91, 123011
 Ewall-Wice, A., et al. submitted 2015, Submitted to *MNRAS*
 Furlanetto, S. R., Oh, S. P., & Briggs, F. H. 2006, *Phys. Rep.*, 433, 181
 Greenhill, L. J., & Bernardi, G. 2012, *ArXiv e-prints*
 Liu, A., Parsons, A. R., & Trott, C. M. 2014a, *Phys. Rev. D*, 90, 023018
 —. 2014b, *Phys. Rev. D*, 90, 023019
 Liu, A., & Tegmark, M. 2011, *Phys. Rev. D*, 83, 103006
 Morales, M. F., & Hewitt, J. 2004, *ApJ*, 615, 7
 Morales, M. F., & Wyithe, J. S. B. 2010, *ARA&A*, 48, 127
 Neben et al. submitted, *ApJ*
 Paciga, G., et al. 2013, *MNRAS*, 433, 639
 Parsons, A. R., Pofer, J. C., Aguirre, J. E., Carilli, C. L., Jacobs, D. C., & Moore, D. F. 2012, *ApJ*, 756, 165

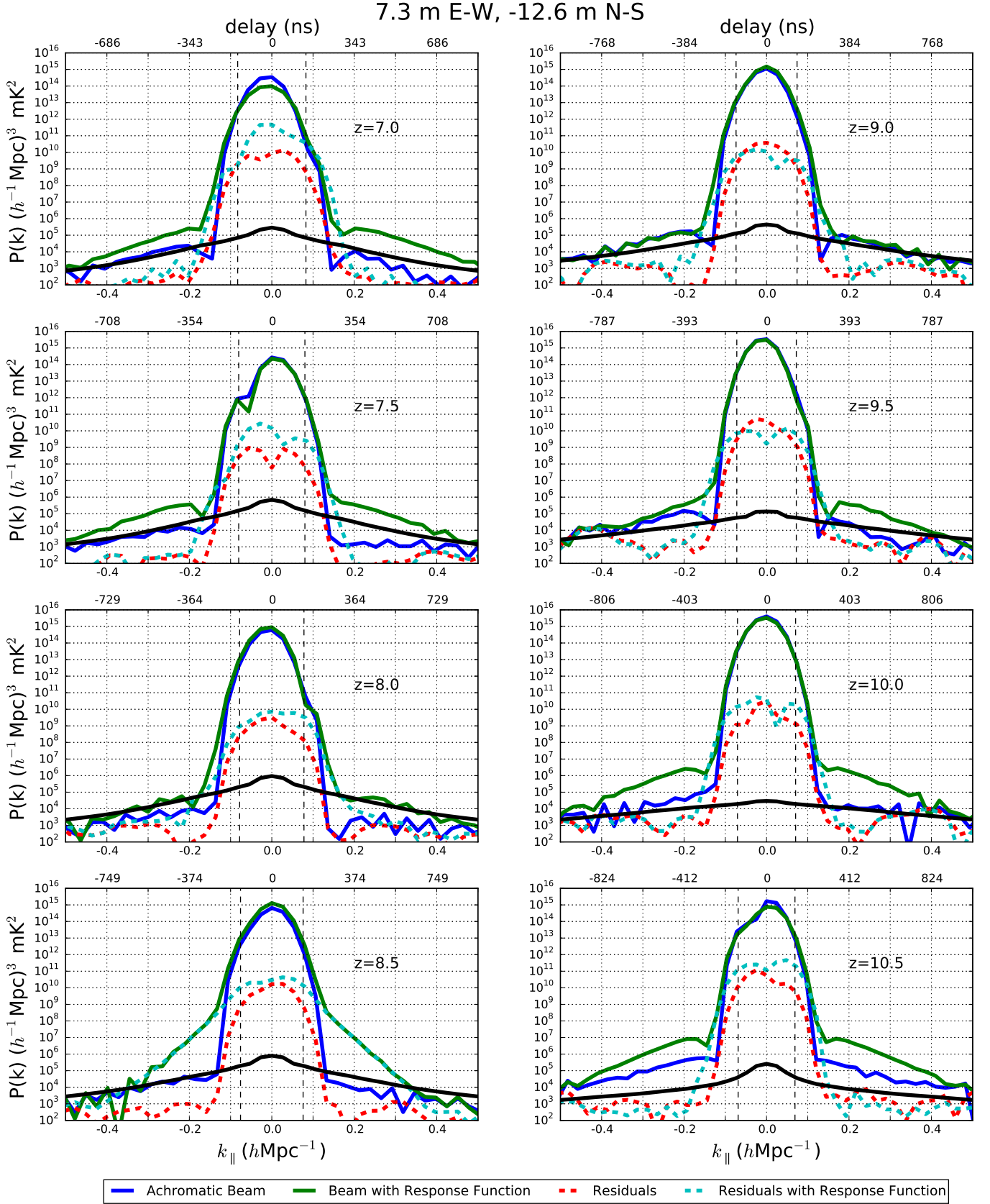


FIG. 11.— The power spectrum computed from the delay transform of a 14.6 meter baseline in equation 20 with (solid green line) and without (solid blue line) the presence of reflections in the HERA dish. The residuals after cleaning within the dashed black lines down to three times the level of thermal noise after 20 minutes of integration with (dashed cyan) and without (red dashed) the dish chromaticity are also plotted. We find that for this short baseline, clean residuals are on a similar level as the 21 cm signal (solid black line), indicating that a redesign of the array with fewer short baselines may be necessary to maximize its sensitivity on foreground free modes.

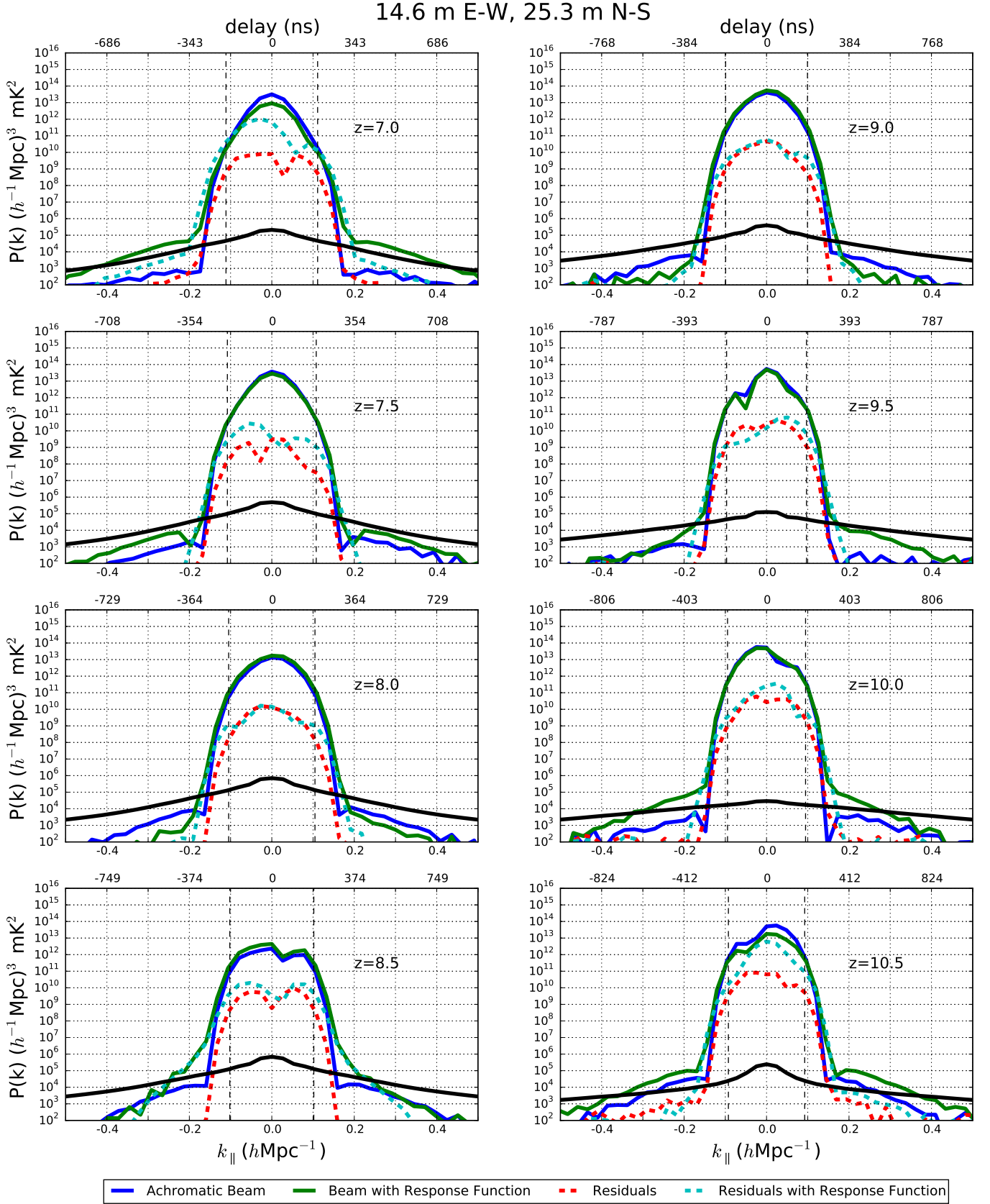


FIG. 12.— The same as Fig. ?? except now for a 29.2 meter baseline. We see that the level of foregrounds is down relative to our 14.6 meter baseline by two orders of magnitude, likely due to the fact that we are now outside of the region with significant contamination from the Galaxy. The presence of reflections tends to extend the k_{\parallel} at which foregrounds drop below the level of the signal between $k_{\parallel} = 0.15 \text{ hMpc}^{-1}$ and $k_{\parallel} = 0.22 \text{ hMpc}^{-1}$ with the most severe contamination occurring at the $z = 8.5$ subband where the reflections were observed to be worst in Fig. 9.

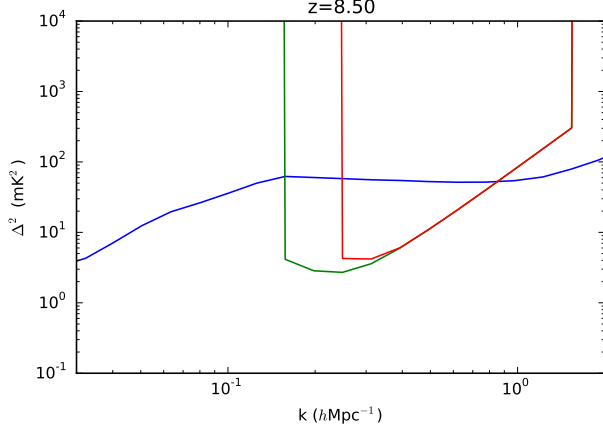


FIG. 13.— Comparison between sensitivities with and without reflections.

Parsons, A. R., et al. 2010, *AJ*, 139, 1468
 Patra et al. submitted, *ApJ*
 Poher, J. C., et al. 2014, *ApJ*, 782, 66
 Pritchard, J. R., & Loeb, A. 2012, *Reports on Progress in Physics*, 75, 086901
 Sokolowski, M., et al. 2015, *PASA*, 32, 4
 Thyagarajan, N., et al. 2013, *ApJ*, 776, 6
 —. 2015a, *ApJ*, 807, L28
 —. 2015b, *ApJ*, 804, 14
 Thyagarajan et al. submitted, *ApJ*
 van Haarlem, M. P., et al. 2013, *A&A*, 556, A2
 Vedantham, H., Udaya Shankar, N., & Subrahmanyam, R. 2012, *ApJ*, 745, 176
 Voytek, T. C., Natarajan, A., Jáuregui García, J. M., Peterson, J. B., & López-Cruz, O. 2014, *ApJ*, 782, L9
 Wieringa, M. H. 1992, *Experimental Astronomy*, 2, 203
 Zheng, H., et al. 2014, *MNRAS*, 445, 1084

APPENDIX

THE EFFECT OF REFLECTIONS AND CROSS-TALK ON VISIBILITIES

In this section, we investigate, formally, the impact of reflections of electromagnetic waves between antennas and within the signal chain of single antennas on foreground leakage in 21 cm experiments. We start with the time varying electric field from a single source with location $\hat{\mathbf{k}}$ on the sky, arriving at antenna i with delay τ_i and antenna j with delay τ_j with respect to the electric field at the origin which we denote as $s(t, \hat{\mathbf{s}})$. We allow for two different types of reflections: First, we allow reflections within the analogue path of each i^{th} antenna which we denote as $r_i(\tau, \hat{\mathbf{s}})$. We also allow for single reflections between any $i-j$ antenna pair which we denote as $r_{ij}(\tau', \hat{\mathbf{s}})$. Our choice of arbitrary τ' , for now, allows for multi-path propagation between antennas, though we expect it to be dominated by the geometrical delay between the antenna pair. The electric field at antenna i is given by

$$s_i(t, \hat{\mathbf{s}}) = \int d\tau' r_i(\tau', \hat{\mathbf{s}}) s(t + \tau_i - \tau') + \sum_{j \neq i} \int d\tau' s(t + \tau_j - \tau_{ij}) r_{ij}(\tau', \hat{\mathbf{s}}) \quad (\text{A1})$$

In an FX correlator, the electric field is sampled, Fourier transformed, and cross multiplied between antenna pairs to form visibilities. The Fourier transform step leaves us with

$$\tilde{s}_i(f, \hat{\mathbf{s}}) = \tilde{s}(f, \hat{\mathbf{s}}) \left[\int d\tau' r_i(\tau', \hat{\mathbf{s}}) e^{2\pi i(\tau_i - \tau')f} + \sum_{j \neq i} \int d\tau' e^{2\pi i(\tau_j - \tau_{ij})f} r_{ij}(\tau', \hat{\mathbf{s}}) \right] \quad (\text{A2})$$

Multiplying and averaging gives us the visibility for the single source we obtain

$$\begin{aligned} v'_{ij}(f, \hat{\mathbf{s}}) &= \langle \tilde{s}_i(f, \hat{\mathbf{k}}) \tilde{s}_j(f, \hat{\mathbf{s}}) \rangle_t \\ &= d\Omega I(f, \hat{\mathbf{s}}) g_i(f) g_j^*(f) a_i(f, \hat{\mathbf{s}}) a_j^*(f, \hat{\mathbf{s}}) e^{2\pi i \mathbf{u}_{ij} \cdot \hat{\mathbf{s}}} + d\Omega I(f, \hat{\mathbf{s}}) \sum_{\ell \neq j} g_i(f) a_i(f, \hat{\mathbf{s}}) C_{\ell j}^*(f, \hat{\mathbf{s}}) e^{2\pi i \mathbf{u}_{\ell i} \cdot \hat{\mathbf{s}}} \\ &\quad + d\Omega I(f, \hat{\mathbf{s}}) \sum_{k \neq i} g_j^*(f) a_j^*(f) C_{ki}(f, \hat{\mathbf{s}}) e^{2\pi i \mathbf{u}_{kj} \cdot \hat{\mathbf{s}}} + d\Omega I(f, \hat{\mathbf{s}}) \sum_{k \neq i} \sum_{\ell \neq j} C_{ki}(f, \hat{\mathbf{s}}) C_{j\ell}^*(f, \hat{\mathbf{s}}) e^{2\pi i \mathbf{u}_{k\ell} \cdot \hat{\mathbf{s}}}, \end{aligned} \quad (\text{A3})$$

where $g_i(f) a_i(f, \hat{\mathbf{s}}) = \int d\tau r_i(\tau, \hat{\mathbf{s}}) e^{2\pi i f \tau}$ is the effective direction dependent gain of the system which can be factored into a direction dependent and direction independent function where $g_i(f)$ is the gain of the analogue signal chain after the radiation has been absorbed by the feed and $a_i(f, \hat{\mathbf{s}})$ describes the chromatic electric field response of the antenna. The first term in equation A3 is an effective visibility with self-reflections. The two cross terms and the last term involve the mixing of visibilities complementary to the ij baseline and have the potential to introduce significant chromatic features since they potentially insert visibilities on much longer baseline lengths. Assuming propagation along a single path directly between the antennas, we may write $C_{ik}(f, \hat{\mathbf{s}})$ as

$$C_{ki}(f, \hat{\mathbf{s}}) = a_i(f, \hat{\mathbf{s}}_{ki}) \frac{1}{r_{ik}} \left[\frac{d\sigma_k}{d\Omega}(f, \hat{\mathbf{s}}, \hat{\mathbf{s}}_{ik}) \right]^{1/2} e^{2\pi i \tau_{ik} f} \quad (\text{A4})$$

Where r_{ik} is the distance between antennas i and k , $d\sigma_k(f, \hat{\mathbf{s}}, \hat{\mathbf{s}}_{ik})/d\Omega$ is the cross-section of the antenna to scatter radiation from the $\hat{\mathbf{s}}$ direction to the $\hat{\mathbf{s}}_{ik}$ direction where $\hat{\mathbf{s}}_{ik}$ is the unit vector in the direction between antenna i and

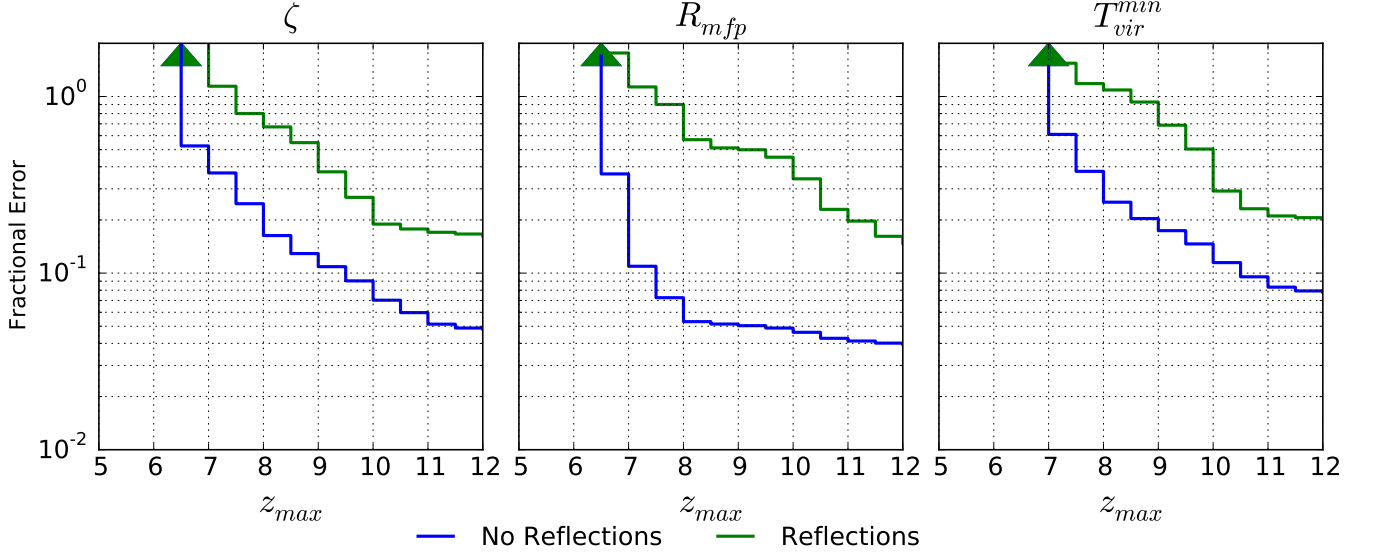


FIG. 14.— Fractional Errors on reionization and heating parameters as a function of maximal observed redshift.

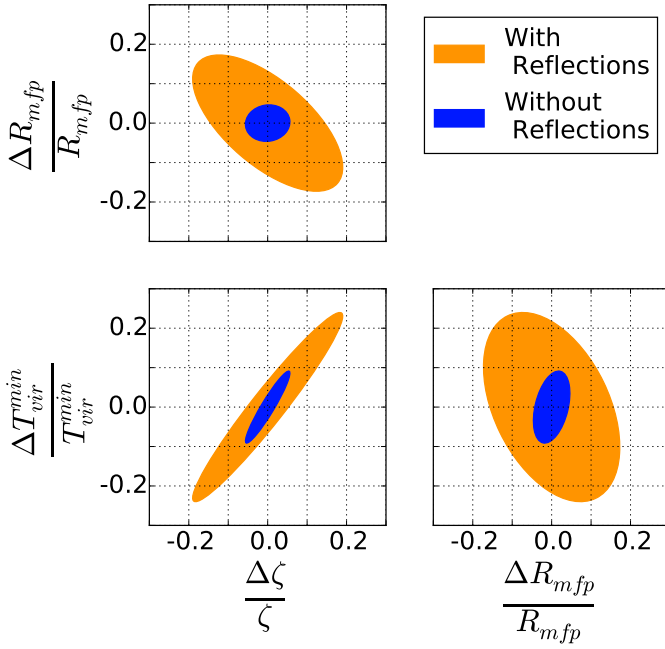


FIG. 15.— 95% confidence regions with and without reflections assuming that observations are taken over the redshifts between 5 and 25 are observed.

antenna k . Integrating over the primary beam, we obtain a full expression on the effect of the foregrounds.

$$V'_{ij} = \int d\Omega v'_{ij}(f, \hat{\mathbf{s}}) = g_i(f)g_j(f)^* \int d\Omega A_{ij}(f, \hat{\mathbf{s}})I(f, \hat{\mathbf{s}})e^{2\pi i f \mathbf{u}_{ij} \cdot \hat{\mathbf{s}}} + g_i(f) \sum_{\ell \neq j} \int d\Omega A_{i\ell j}(f, \hat{\mathbf{s}})I(f, \hat{\mathbf{s}})e^{2\pi i \mathbf{u}_{i\ell} \cdot \hat{\mathbf{s}}} \\ + g_j^*(f) \sum_{k \neq i} \int d\Omega A_{jki}^*(f, \hat{\mathbf{s}})I(\hat{\mathbf{s}}, f)e^{2\pi i \mathbf{u}_{kj} \cdot \hat{\mathbf{s}}} + \sum_{k \neq i} \sum_{\ell \neq j} \int d\Omega A_{k\ell j}(f, \hat{\mathbf{s}})I(f, \hat{\mathbf{s}})e^{2\pi i \mathbf{u}_{k\ell} \cdot \hat{\mathbf{s}}} \quad (\text{A5})$$

which is essentially an ad-mixture of many baselines with different effective primary beams. We denote the effective primary beam of the i, j antenna pair as $A_{ij}(f, \hat{\mathbf{s}}) = a_i(f, \hat{\mathbf{s}})a_j^*(f, \hat{\mathbf{s}})$, the effective beam from a single reflection correlated with a direct measurement as $A_{i\ell j} = a_i(f, \hat{\mathbf{s}})C_{\ell j}^*(f, \hat{\mathbf{s}})$ and the correlation between entirely reflected terms as experiencing an effective primary beam of $A_{k\ell j} = C_{ki}(f, \hat{\mathbf{s}})C_{j\ell}^*(f, \hat{\mathbf{s}})$. In this paper, we focus on the reflection terms within a single antenna element. Hence, we ignore all but the first term for now. Any reflection terms occurring downstream of the conversion by the feed from electromagnetic radiation to voltage are lumped into $g_i(f)$ and reflections occurring within the antenna element enter into $a_i(f, \hat{\mathbf{s}})$. While reflections within the analogue system are a potential source of contamination, HERA's post-feed analogue signal path is designed to keep all reflections under 35 m, within the wedge.

The focus of this paper and its companions is the reflection properties of the primary antenna element, so we will focus the rest of our discussion here on $a_i(f, \hat{\mathbf{s}})$. The primary elements of our dish include a feed and backplane suspended over a fourteen meter dish. We assume a set of discrete reflections within the dish, which without loss of generality are assumed to have frequency independent reflection coefficients⁸ hence

$$a_i(f, \hat{\mathbf{s}}) = \sum_n r_n(\hat{\mathbf{s}})e^{2\pi i \tau_n f} \quad (\text{A6})$$

Assuming all antennas are identical, we have

$$A_{ij}(f, \hat{\mathbf{s}}) = \sum_m \sum_n r_n(\hat{\mathbf{s}})r_m^*(\hat{\mathbf{s}})e^{2\pi i(\tau_n - \tau_m)f} = \sum_\alpha A_\alpha(\hat{\mathbf{s}})e^{2\pi i \tau_\alpha f} \quad (\text{A7})$$

where we have re-indexed m and n under a single greek index α in the second equality. The effect of internal reflections on a visibility is hence

$$V'_{ij} = \sum_\alpha \int d\Omega A_\alpha(\hat{\mathbf{s}})e^{2\pi i \tau_\alpha f} e^{2\pi i \mathbf{b}_{ij} \cdot \hat{\mathbf{s}} f/c} I(f, \hat{\mathbf{s}}) \quad (\text{A8})$$

Taking the delay transform, one obtains

$$\tilde{V}'_{ij}(\tau) = \sum_\alpha \tilde{V}_{ij}^\alpha(\tau - \tau_\alpha) \quad (\text{A9})$$

where

$$\tilde{V}_{ij}^\alpha(\tau) = \int d\tau e^{-2\pi i f \tau} \int d\Omega A_\alpha(\hat{\mathbf{s}})e^{2\pi i \mathbf{b}_{ij} \cdot \hat{\mathbf{s}} f/c} I(f, \hat{\mathbf{s}}) \quad (\text{A10})$$

is the usual delay transform of Parsons et al. (2012). $\tilde{V}_{ij}^{alpha}(\tau)$.

⁸ If we allow each coefficient to be frequency dependent, we can expand each frequency dependent term in a Fourier series of

frequency independent terms